

A Fast and Stable Feature-Aware Motion Blur Filter

Jean-Philippe Guertin, Morgan McGuire, and Derek Nowrouzezahrai

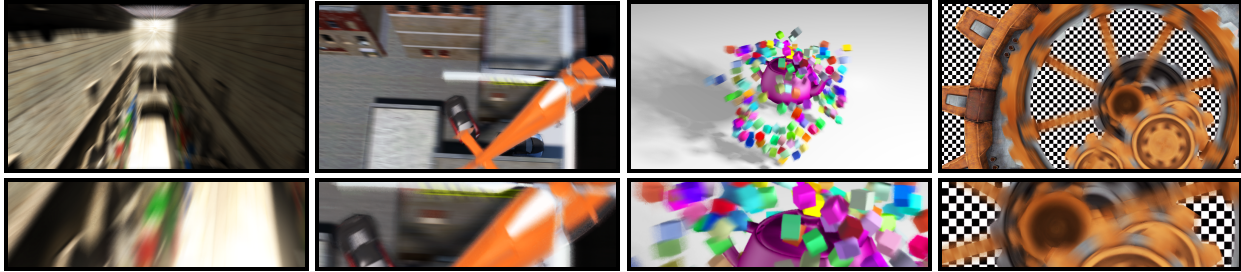


Figure 1: We render temporally coherent motion blur without any motion artifacts, even on animation sequences with complex depth and motion relationships that are challenging for previous post-process techniques. All results are computed in about 3ms at 1280×720 on a GeForce GTX480, and our filter integrates seamlessly with post-process anti-aliasing and depth of field.

Abstract

High-quality motion blur is an increasingly important and pervasive effect in interactive graphics that, even in the context of offline rendering, is often approximated using a post process. Recent motion blur post-process filters (e.g., [MHBO12, Sou13]) efficiently generate plausible results suitable for modern interactive rendering pipelines. However, these approaches may produce distracting artifacts, for instance, when different motions overlap in depth or when both large- and fine-scale features undergo motion. We address these artifacts with a more robust sampling and filtering scheme that incurs only small additional runtime cost. We render plausible, temporally-coherent motion blur on several complex animation sequences, all in just 3ms at a resolution 1280×720 . Moreover, our filter is designed to integrate seamlessly with post-process anti-aliasing and depth of field.

Categories and Subject Descriptors (according to ACM CCS): I.3.7 [Computer Graphics]: Three-Dimensional Graphics and Realism—Color, shading, shadowing, and texture

1. Introduction

Motion blur is an essential effect in realistic image synthesis, providing important motion cues and directing viewing attention, and is one of the few effects that distinguishes high-quality film production renderings from interactive graphics. We phenomenologically model the perceptual cues of motion blurred image sequences to approximate this effect with high quality using a simple, high-performance post-process.

We are motivated by work in offline motion blur post-processing [Coo86, ETH*09, LAC*11], where many of the initial experiments applied reconstruction filters to stochastic sampling routines. Unfortunately, these approaches are too heavyweight for modern game engines, however many of their ideas remain useful. Conversely, adhoc approaches (e.g., applying a Gaussian blur to moving objects) have existed in various forms for several years, however the question of how to approach motion blur post-processing using a well-founded methodology has only recently gained atten-

tion in the interactive rendering community. This methodology had first found use (and success) in post-process anti-aliasing [Lot09] and depth of field [Eng06] approaches. We target temporally-coherent and plausible high-quality motion blur that rivals super-sampled results, but on a small performance budget and a simple implementation. As such, we build upon recent post-process motion blur filters [MHBO12, Sou13] and address several of their limitations in order to produce high-performance, stable, feature-preserving and plausible motion blurred image sequences.

Contributions. Previous works rely on conservative assumptions about local velocity distributions at each pixel in order to apply plausible, yet efficient, blurs. Unfortunately, distracting artifacts arise when these assumptions are broken; this occurs when objects nearby in image-space move with different velocities, which is unavoidable even in simple scenes, or when objects under (relative) motion have geometric features of different scales. We eliminate these ar-

tifacts and compute stable motion blur for both simple and complex animation configurations. Our contributions are:

- an improved, variance-driven directional sampling scheme that handles anisotropic velocity distributions,
- a sample-weighting scheme that preserves unblurred object details and captures fine- and large-scale blurring, and
- a more robust treatment of tile boundaries, and interaction with post-process anti-aliasing and depth of field.

We operate on g-buffers, captured at a single time instance, with standard rasterization. Our results are stable under animation, robustly handle complex motion scenarios, and all in about 3ms per frame (Figure 1). Since ours is an image post-process filter, it can readily be used in an art-driven context to generate non-physical and exaggerated motion blur effects. We provide our full pseudocode in Appendix A.

2. Previous Work and Preliminaries

Given the extensive work on motion blur, we discuss recent work most related to our approach and refer interested readers to a recent survey on the topic [NSG11].

Sampling Analysis and Reconstruction. Cook’s seminal work on distribution effects [Coo86] was the first to apply different (image) filters to reduce artifacts in the context of stochastic ray-tracing and micropolygon rasterization. More recent approaches filter noise while retaining important visual details, operating in the multi-dimensional primal [HJW*08], wavelet [ODR09] or data-driven [SD12] domains. Egan et al. [ETH*09] specifically analyze the effects of sample placement and filtering, in the frequency domain of object motion, and propose sheared reconstruction filters that operate on stochastically distributed spatio-temporal samples. Lehtinen et al. [LAC*11] use sparse samples in ray-space to reconstruct the anisotropy of the spatio-temporal light-field at a pixel and reconstruct a filtered pixel value for distribution effects. These latter two techniques aim to minimize integration error given fixed sampling budgets in stochastic rendering engines. We also reduce visible artifacts due to low-sampling rates, however we limit ourselves to interactive graphics pipelines where distributed temporal sampling is not an option and where compute budgets are on the order of milliseconds, not minutes.

Stochastic Rasterization. Recent work on extending triangle rasterization to support the temporal- and lens-domains [AMMH07], balances the advantages and disadvantages of GPU rasterization, stochastic ray-tracing, and modern GPU micropolygon renderers [FLB*09]. Here, camera-visibility and shading are evaluated at many samples in space-lens-time. Even with efficient implementations on conventional GPU pipelines [MESL10], these approaches remain too costly for modern interactive graphics applications. Still, Shirley et al. [SAC*11] discuss image-space filters for plausible motion blur given spatio-temporal output

from such stochastic multi-sample renderers. We are motivated by their phenomenological analysis of motion blur behaviour and extend their analysis to more robustly handle complex motion scenarios (see Section 4).

Interactive Heuristics. Some approaches blur albedo textures prior to texture mapping (static) geometry [Lov05] or extrude object geometry using shaders [TBI03], however neither approach properly handles silhouette blurring, resulting in unrealistic motion blur. Max and Lerner [ML85], and Pepper [Pep03], sort objects by depth, blur along their velocities, and compose the result in the final image, but this strategy fails when a scene invalidates the painter’s visibility assumption. Per-pixel variants of this approach can reduce artifacts [Ros08, RMM10], especially when image velocities are dilated prior to sampling [Sou11, KS11], however this can corrupt background details and important motion features when multiple objects are present.

Motivated by recent tile-based, *single blur velocity* approaches [Len10, MHBO12, ZG12, Sou13] (see Section 3), we also dilate velocities to reason about large-scale motion behavior while sampling from the original velocity field to reason about the spatially-varying blur we apply. However, we additionally incorporate higher-order motion information and feature-aware sample weighting to produce results that are stable and robust to complex motion, effectively eliminating the artifacts present in the aforementioned “*single-velocity*” approaches. Specifically, we robustly handle:

- interactions between many moving and static objects,
- complex temporally-varying depth relationships,
- correct blurring regardless of object size or tile-alignment,
- feature-preservation for static objects/backgrounds.

We build atop existing state-of-the-art tile-based plausible motion blur approaches, detailed in Section 3, and present our more robust *multi-velocity* extensions in Section 4.

3. Tile-Based Dominant Velocity Filtering Overview

We base our approach on recent **single-velocity** techniques [Len10, MHBO12, ZG12, Sou13] that combine phenomenological motion analysis and sampling-aware reconstruction filters. Figure 2 outlines the operation of these approaches: first, the image is split into square $r \times r$ tiles according to a maximum blur radius r in image-space, ensuring that each pixel can at most be influenced by its (1-ring) neighboring tiles; secondly, a *single* dominant neighborhood velocity direction is determined at each tile; finally, the color at the pixel is combined with weighted color samples along the dominant blur direction.

We review some notable details of this approach below:

- a tile’s dominant velocity \mathbf{v}_{\max} (Figure 2b; green) is computed in two steps: *maximum* per-pixel velocities are retained per-tile (Figure 2a,b; green, blue), and a 1-ring *maximum* of the per-tile maxima yields \mathbf{v}_{\max} ,

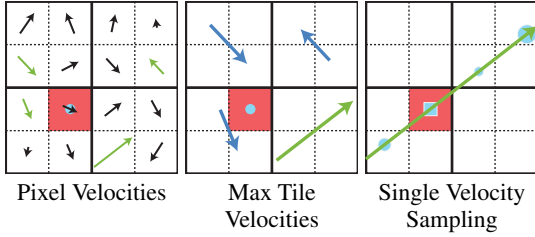


Figure 2: Motion blur with “single-velocity” techniques.

- pixels are sampled *exclusively* along \mathbf{v}_{\max} , yielding high cache coherence but ignoring complex motions, and
- each sample’s weight is computed using a depth-aware metric that only considers the *magnitude* of velocities at the source and sample points.

The “TileMax” pass can be computed in two passes, one per image dimension, to greatly improve performance at the cost of a slight increase in memory usage. Samples are jittered to reduce (but not eliminate; see Section 4.5) banding, and samples are weighted (Figure 2c) to reproduce the following phenomenological motion effects:

1. a distant pixel/object blurring over the shading pixel,
2. transparency at the shading pixel from its motion, and
3. the proper depth-aware combination of effects 1 and 2.

These techniques generate plausible motion blur with a simple, high-performance post-process and have thus already been adopted in production game engines; however, the single dominant velocity assumption, coupled with the sample weighting scheme, results in noticeable visual artifacts that limit their ability to properly handle: overlapping objects that move in different directions, tile boundaries, and thin objects (see Figures 3, 6, 7, 11, 12 and 15).

We identify, explain, and evaluate new solutions for these limitations. We follow the well-founded phenomenological methodology established by *single-velocity* approaches and other prior work [Len10, SAC*11, MHBO12, ZG12, Sou13], and our technique maintains high cache coherence and parallelizable divergence-free computation for an equally simple and high-performance implementation.

4. Stable and Robust Feature-Aware Motion Blur

We motivate our improvements by presenting artifacts in existing (single-velocity) approaches. We demonstrate clear improvements in visual quality with negligible additional cost. Furthermore, our supplemental video illustrates the stability of our solution under animation and on scenes with complex geometry, depth, velocity and texture.

4.1. Several Influential Motion Vectors.

The *dominant velocity* assumption breaks down when a tile contains pixels with many different velocities, resulting in

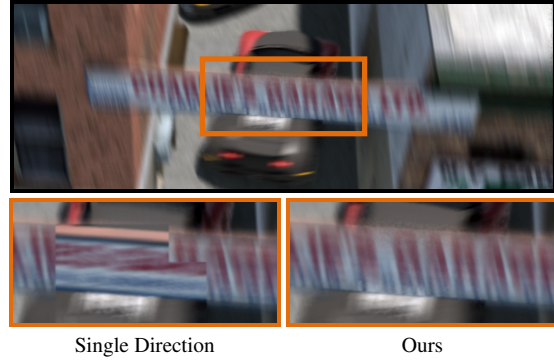


Figure 3: Top: an animation with complex depth and motion relationships. The camera is moving upwards and the car is doing a sharp turn while moving up. Bottom: single-velocity approaches (left) cannot handle these cases, resulting in distracting artifacts both inside and between tiles; our filter (right) generates the correct plausible blur and is temporally stable (see video).

both an incorrect blur *inside* a tile and blur mismatches *between* tiles (see Figures 3 and 6). This can occur, for example, with rotating objects (see Figure 7), objects with features smaller than a tile (see Figure 11), or when the view and motion directions are (nearly) parallel (see Figure 6).

Specifically, by exploiting this assumption to reduce the sampling domain to 1D, *single-velocity* approaches weight samples along \mathbf{v}_{\max} according only to the *magnitudes* of their velocities, and not the *directions*. This can result in overblurred shading when samples (that lie along the dominant direction) should otherwise not contribute to the pixel but are still factored into the sum, especially if they are moving quickly (i.e., have large velocity magnitudes).

To reduce these artifacts we sample along a second, carefully chosen direction. Moreover, we split samples between these two directions according to the variance in the neighborhood’s velocities, while also weighting samples using a locally-adaptive metric based on the deviation of sample velocities from the blur direction. This scheme better resolves complex motion details and still retains cache coherence by sampling along (fixed) 1D domains. Section 5 details our algorithm and we provide pseudocode in Appendix A.

Local Velocity Sampling. If a pixel’s velocity differs significantly from the dominant direction, then it should also be considered during sampling. As such, we sample along both the pixel’s velocity and the dominant velocity directions. This immediately improves the blur for scenes with complex pixel- and neighborhood-velocity relationships (e.g., Figure 3), however at the cost of increased noise since we are effectively halving the sampling rate in each 1D sub-domain.

If the pixel’s velocity is negligible, this scheme effectively “wastes” all the integration samples placed on the second direction. In these cases, we replace the pixel’s velocity with

the velocity *perpendicular* to the dominant direction, sampling along this new vector for half of the total samples and in the dominant direction for the other half. This helps in scenarios where the dominant velocity entirely masks smaller velocities with different directions, in the neighborhood, and the perpendicular direction serves as a "best-guess" to maximize the probability of sampling along an otherwise ignored important direction. Of course, if no such important (albeit secondary) direction exists, then we are left with a similar situation where samples placed along this perpendicular direction are "wasted".

We ultimately combine the ideas of pixel ($\mathbf{v}(\mathbf{p})$) and perpendicular-dominant ($\mathbf{v}_{\max}(\mathbf{t})$) velocities at the shading pixel \mathbf{p} 's tile \mathbf{t} : we place a number (discussed below) of samples along the *center direction* that interpolates between $\mathbf{v}(\mathbf{p})$ and $\mathbf{v}_{\max}^{\perp}(\mathbf{t})$ as the pixel's velocity diminishes past a minimum user threshold γ (see Figure 4),

$$\mathbf{v}_c(\mathbf{p}) = \text{lerp}\left(\mathbf{v}(\mathbf{p}), \mathbf{v}_{\max}^{\perp}(\mathbf{t}), (\|\mathbf{v}(\mathbf{p})\| - 0.5)/\gamma\right). \quad (1)$$

Sampling along both $\mathbf{v}_{\max}(\mathbf{t})$ and $\mathbf{v}_c(\mathbf{p})$ ensures that each sample contributes usefully to the final blur, better capturing complex motion effects. This approach remains robust when the pixel's velocity is low (or zero, for static objects; see Figures 3 and 6).

The number of samples we place along \mathbf{v}_c , and their weights (both along \mathbf{v}_c and \mathbf{v}_{\max}), plays an important role in the behavior and quality of the motion blur. We address the problems of assigning samples to each direction, and weighting them, separately. We first discuss the distribution of samples over these two directions, and only later discuss a more accurate scheme for weighting their individual contributions. Our final sampling scheme is robust to complex scenes and stable under animation.

Tile Variance for Sample Assignment. We first address the segmentation and assignment of samples to \mathbf{v}_c and \mathbf{v}_{\max} . In cases where the dominant velocity assumption holds, we should sample *exclusively* from \mathbf{v}_{\max} , as the standard *single-velocity* approaches [Len10, MHBO12, ZG12, Sou13] do; however, it is rare that this assumption holds *completely* and we would like to find the ideal assignment of samples to the two directions in order to simultaneously capture more complex motions while reducing noise. This amounts

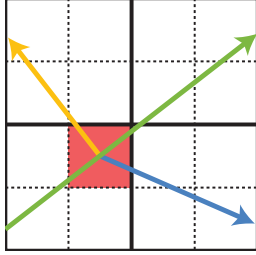


Figure 4: Sampling directions \mathbf{v}_{\max} (green), $\mathbf{v}_{\max}^{\perp}$ (yellow) and $\mathbf{v}(\mathbf{p})$ (blue).

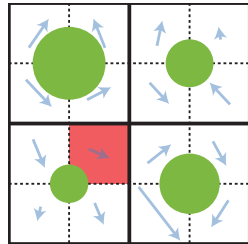


Figure 5: Variance (green) for tiles neighboring the pixel \mathbf{p} (red).

to minimizing the number of "wasted" samples. To do so, we propose a simple variance estimation metric.

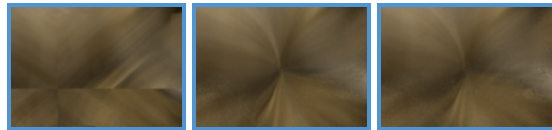
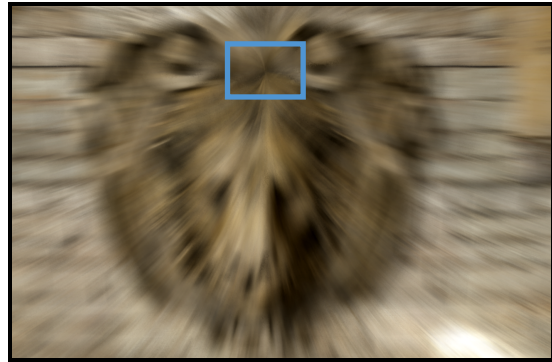
At each tile, we first compute the angular variation between a tile's and its neighbor's maximum velocities as

$$\upsilon(\mathbf{t}) = 1 - \frac{1}{|\mathcal{N}|} \sum_{\mathbf{t} \in \mathcal{N}} \text{abs}[\mathbf{v}_{\max}(\mathbf{t})] \cdot \text{abs}[\mathbf{v}_{\max}(\bar{\mathbf{t}})] , \quad (2)$$

where \mathcal{N} is the (1-ring) neighborhood tile set around (and including) \mathbf{t} . The variance $0 \leq \upsilon \leq 1$ is larger when neighboring tile velocities differ from $\mathbf{v}_{\max}(\mathbf{t})$, and smaller when they do not. As such, we can use $\upsilon(\mathbf{t})$ to determine the number of samples assigned to \mathbf{v}_c and \mathbf{v}_{\max} with: $\upsilon \times N$ assigned to \mathbf{v}_c and $(1 - \upsilon) \times N$ assigned to \mathbf{v}_{\max} (Figure 5).

This metric works well in practice, significantly reducing distracting visual artifacts near complex motion while gracefully reverting to distributing fewer samples along \mathbf{v}_c when the motion is simple; however, we require an extra (reduced-resolution) render pass (and texture) to compute (and store) υ , which is less than ideal for pipeline integration (albeit with negligible performance impact). We observe in practice that, while the variance-based sample assignment does improve the quality of the result, conservatively splitting our samples evenly between \mathbf{v}_c and \mathbf{v}_{\max} (i.e., $N/2$ samples for each) generates roughly equal quality results (see Figure 6).

We note, however, that the *weighting* of each sample plays a sizeable role in both the quality of the final result and the ability to properly and consistently reconstruct complex motion blurs. We detail our new weighting scheme and contrast it to the scheme used in prior *single-velocity* approaches.



Single Direction Variance Velocity Direction

Figure 6: The lion in Sponza moving directly towards the viewer. Bottom: single-velocity results (left), our variance-based sample distribution (middle) conservative sample distribution (right) both with \mathbf{v}_{\max} and \mathbf{v}_c direction sampling.

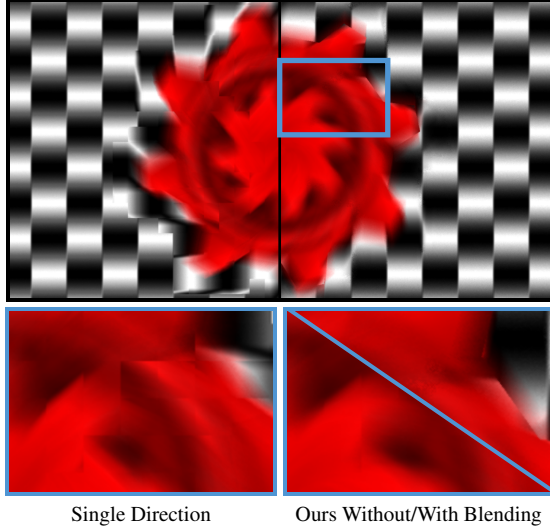


Figure 7: Tile edge artifacts. Bottom: single-velocity blurring (left) results in disturbing tile-edge artifacts that are reduced, in part, using multi-direction sampling (right; bottom) and, in full, with stochastic \mathbf{v}_{\max} blending (right; top).

Feature-Aware Sample Weights. Single-velocity approaches compute weights by combining two metrics:

- depth difference between the sampled position and \mathbf{p} , and
- the *magnitude* of the velocity at the sample point and at \mathbf{p} .

This does not consider that samples can still fall on objects that move in directions different than \mathbf{v}_{\max} (and even \mathbf{v}_c). We instead additionally consider the velocity *direction* at samples when computing their weights. This yields a scheme that more appropriately adapts to fine-scale motions, without complicating the original scheme. Specifically, we will consider the dot product between blurring directions and sampled velocity directions. Recalling the three phenomenological motion blur effects in Section 3, we modify the weights corresponding to each component as follows:

1. the contribution of distant objects blurring onto \mathbf{p} , along the sampling direction, are (additionally) weighted by the dot product between the sample’s velocity direction and the sampling direction (either \mathbf{v}_{\max} or \mathbf{v}_c , as discussed earlier); here, the total weight models the amount of color that blurs from the distant sample onto \mathbf{p} and, as such, can be modulated as the velocity at the sample \mathbf{v}_s differs from the blurring/sampling direction,
2. the transparency caused by \mathbf{p} ’s blur onto its surrounding is (additionally) weighted by the dot product of its velocity (actually, \mathbf{v}_c) and the dominant blur direction \mathbf{v}_{\max} ; here, the total weight models the visibility of the background behind the pixel/object at \mathbf{p} and, as such, if \mathbf{v}_c differs from \mathbf{v}_{\max} , the contribution should reduce appropriately, and
3. the *single-velocity* approaches include a correction term to both model the combination of the two blurring effects above and also account for discontinuities along object

edges; we (additionally) multiply the weight for this term by the *maximum* of the two dot products above; here, the maximum is a conservative estimate that errs on the side of slightly oversmoothing any such edges.

These simple changes (see pseudocode in Appendix A) significantly improve quality within and between tiles, particularly when many motion directions are present (Figure 6).

4.2. Tile Boundary Discontinuities.

The tile-based nature of *single-velocity* approaches, combined with their exclusive dependence on the dominant velocity, can easily lead to distracting tile-boundary discontinuities when blur directions vary significantly between tiles (see Figure 7). This occurs when \mathbf{v}_{\max} differs significantly between adjacent tiles and, since the original approach samples *exclusively* along \mathbf{v}_{\max} , neighboring tiles can end up being blurred in completely different directions. Our sampling and weighting approaches (Section 4.1) already help to reduce this artifact, but we continue to sample from \mathbf{v}_{\max} (albeit not exclusively, and with a different weighing scheme), and so we remain sensitive (to a lesser extent) to quick changes in \mathbf{v}_{\max} (see Figures 9 and 7).

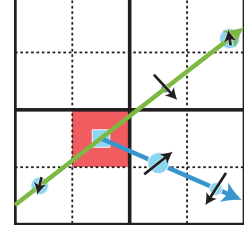


Figure 8: Adapting per-sample weights according to the fine-scale velocity information.

To further reduce this artifact, we stochastically offset our lookup into the NeighborMax maximum neighborhood velocity texture for pixels near a tile edge. This effectively trades banding for noise in the image, around tile boundaries, along edges in the \mathbf{v}_{\max} buffer. Thus, the probability of sampling along the \mathbf{v}_{\max} of a neighboring tile falls off as a pixel’s distance to a tile border increases (Figure 9); we use a simple linear fall-off with a controllable (but fixed; see Section 5) slope τ .

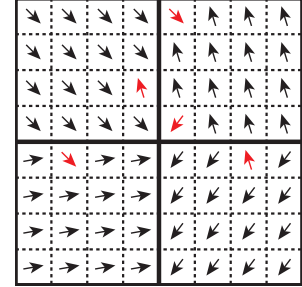


Figure 9: We jitter the $\mathbf{v}_{\max}(t)$ sample with higher probability closer to tile borders.

It is important to note that, while intuitively logical, linearly interpolating between neighborhood velocities along tile edges produces incorrect results. Indeed, not only is the interpolation itself not well-defined (for instance, interpolating two antiparallel velocities requires special care), but even more importantly, two objects blurring on one another with different motion directions is not equivalent to blurring along the average of their directions. Doing so causes distracting

artifacts where the blur seems to wave and often highlights, as opposed to mask, tile boundaries.

4.3. Preserving Thin Features.

Single-velocity filtering ignores the (jittered) mid-point sample closest to the pixel and instead explicitly weighs the color at \mathbf{p} by the *magnitude* of the \mathbf{p} 's velocity, without considering relative depth or velocity information (as with the remaining samples). This was designed to retain some of a pixel's original color regardless of the final blur, but it is not robust to scenes with thin features or large local depth/velocity variation. Underestimating this *center weight* causes thin objects to disappear or "ghost" (see Figure 11). Furthermore, the weight is not normalized and so its effect reduces as N increases. These artifacts are distracting and unrealistic, and the weight's dependence on N makes it difficult to control.

We instead set this *center weight* as $w_p = \|\mathbf{v}\|^{-1} \times N/\kappa$, where κ is a user-parameter to bias its importance. We use $\kappa = 40$ in all of our results (see Section 5 for all parameter settings). The second term in w_p serves as a pseudo-energy conservation normalization, making w_p robust to varying sampling rates N (unlike previous *single-velocity* approaches). Lastly, we do not omit the mid-point sample closest to \mathbf{p} , treating it just as any other sample and applying our modified feature-aware sampling scheme (Section 4.1). As such, we also account for relative velocity variations at the midpoint, resulting in plausible motion blur robust to thin features and to different sampling rates (see Figure 11).

4.4. Neighbor Blurring.

Both our approach and previous *single-velocity* approaches rely on an efficient approximation of the dominant neighborhood velocity \mathbf{v}_{\max} . We present a modification to McGuire et al.'s [MHBO12] scheme that increases robustness by reducing superfluous blur artifacts present when the \mathbf{v}_{\max} estimate deviates from its true value. Specifically, the NeighborMax pass in [MHBO12] conservatively computes the maximum velocity using the eight neighboring tiles (see Section 3 and Figure 2b), which can potentially result in an overestimation of the actual maximum velocity affecting the central tile. We instead only consider a diagonal tile in the \mathbf{v}_{\max} computation if its maximum blur direction would in fact affect the current tile. For instance, if the tile to the top-left of the central tile has a maximum velocity that does not point towards the middle, it is not considered in the \mathbf{v}_{\max} computation (Figure 10). The reasoning is that slight velocity deviations at on-axis tiles can result in

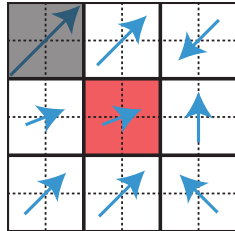


Figure 10: *Off-axis neighbors are only used for \mathbf{v}_{\max} computation if they will blur over the central tile.*

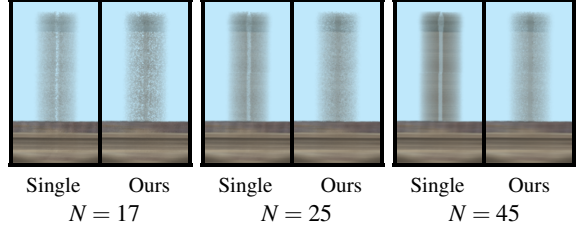


Figure 11: *Thin objects like the flagpole in Sponza ghost, to varying degrees depending on the sampling rate, with the single-velocity approach. Our approach resolves these details and is robust to changes in the sampling rate.*

blurs that overlap the middle tile, however larger deviations are required at the corner (off-axis) tiles.

4.5. Stochastic Noise and Post-Process Anti-Aliasing

We have discussed how to choose the direction along which to place each sample (either \mathbf{v}_{\max} or \mathbf{v}_c) as well as how to weight them (Section 4.1), however we have not discussed *where* to place samples along the 1D domain. Numerical integration approaches are sensitive to sample distribution and, in the case of uniform samples distributed over our 1D domain, the quality of both ours and the *single-velocity* techniques can be significantly influenced by this choice. McGuire et al. [MHBO12] use equally-spaced uniform samples and jitter the pattern at each pixel using a hashed noise texture. This *jittered uniform* distribution has been recently analyzed in the context of 1D shadowing problems with linear lights [RAMN12] where it was proven to reduce variance better than low-discrepancy and stratified sampling.

We modify this strategy for motion blur integration and use a deterministic Halton sequence [WLH97] to jitter the per-pixel sample sets with a larger maximum jitter value η (in pixel units), which improves the quality of the results; furthermore, as discussed earlier, we do not ignore the central sample closest to \mathbf{p} and, as such, properly take its relative depth and local-velocity into account during weighting.

Noise Patterns and Post-Process Anti-Aliasing. The noise patterns produced by our stochastic integration are well-suited as input to post-processed screen-space anti-aliasing methods, such as FXAA. Specifically, per-pixel jitter ensures that wherever there is residual noise, it appears as a high-frequency pattern that triggers the antialiasing luminance edge detector (Figure 13, top right). The post-process antialiasing then blurs each of these pixels (Figure 13, bottom left), yielding a result with quality comparable to roughly double the sampling rate (without FXAA; Figure 13, top left). Stochastic \mathbf{v}_{\max} blending (Section 4.2) is compatible with this effect.

Furthermore, it is possible to maximize the noise smoothing properties of post-processed antialiasing by feeding a

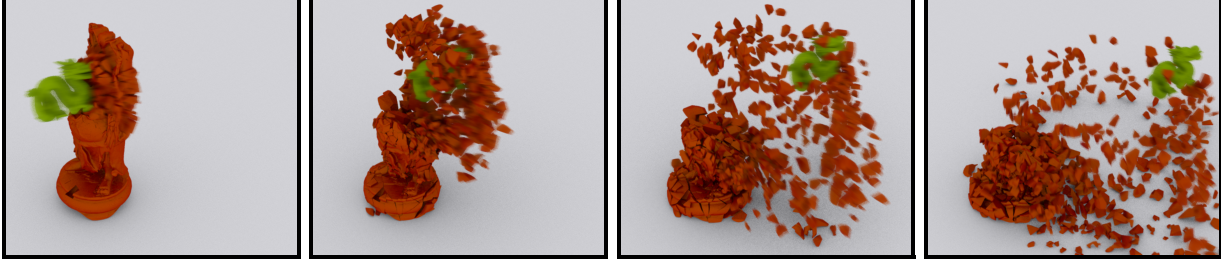


Figure 12: Our motion blur results are temporally coherent and stable even in scenes with turbulent geometric deformation.

maximum-intensity, pixel-sized checkerboard to the edge detector’s luminance input. This causes the antialiasing filter to detect edges on all motion blurred pixels, thus suppressing residual motion blur sampling noise (Figure 13, bottom right).

5. Implementation and Results

All our results are captured live at 1280×720 on an Intel Core i5 at 3.3GHz with 16GB RAM and an NVIDIA GTX480 with 1.5GB vRAM. We recommend that readers digitally zoom-in on our (high-resolution) results to note fine-scale details. Since our filter implementation does not have any divergent code paths our performance, at this resolution, was consistently $3.2\text{ms} \pm 5\%$. We use the same parameter settings for all our scenes: $\{N, r, \tau, \kappa, \eta, \gamma\} = \{25, 40, 1, 40, 0.95, 1.5\}$. All intermediate textures, `TileMax`, `NeighborMax` [MHBO12] and `TileVariance` (Section 4.1), are stored in `UINT8` format and sampled using nearest neighbor interpolation, except for `TileVariance` that required a bilinear interpolant to eliminate residual tile boundary artifacts.

We note the importance of properly quantizing and encoding the per-pixel velocity when using integer buffers for storage (as is typically done in e.g. game engines). Specifically, a limitation in the encoding used in McGuire et al.’s implementation, $V[x, y] = \mathbf{v}(\mathbf{p}_{x,y})/2r + 0.5$, is that the x and y

velocity components are clamped *separately* to $\pm r$, causing large velocities to only take on one of four possible values: $(\pm r, \pm r)$. Instead, we propose a clamping scheme that makes optimal use of an integer buffer’s precision, normalizing according to the range $[-r, r]$ as

$$V[x, y] = \frac{\mathbf{v}(\mathbf{p}_{x,y})}{2r} \times \frac{\max(\min(|\mathbf{v}(\mathbf{p}_{x,y})| \times E, r), 0.5)}{|\mathbf{v}(\mathbf{p}_{x,y})| + \epsilon} + 0.5,$$

where $\epsilon = 10^{-5}$ and the exposure time E is in seconds.

We modify the *continuous depth comparison* function (`zCompare`) used by McGuire et al. to better support depth-aware fore- and background blurring as follows: instead of using a hard-coded, *scene-dependent* depth-transition interval, we use the relative depth interval

$$z\text{Compare}[z_a, z_b] = \min\left(\max\left(0, 1 - \frac{(z_a - z_b)}{\min(z_a, z_b)}\right), 1\right),$$

where z_a and z_b are both depth values. This relative test has important advantages: it works on values in a scene-independent manner, e.g. comparing objects at 10 and 20 z-units will give similar results to objects at 1000 and 2000 z-units. This allows smooth blending between distant objects, compensating for their reduced on-screen velocity coverage, all while remaining robust to arbitrary scene scaling.

Motivated by Sousa’s [Sou13] endorsement of McGuire et al.’s *single-velocity* implementation, which has already been used in several game engines, all our comparisons were conducted against an optimized version of the open source implementation provided by McGuire et al., with both our Halton jittering scheme and our velocity encoding. While the variance-based \mathbf{v} metric for distributing samples between \mathbf{v}_{\max} and \mathbf{v}_c yields slightly improved results over e.g. a 50/50 sample distribution, we observe no perceptual benefit in using \mathbf{v} during interactive animation; as such, we disabled this feature in all our results (except Figure 6, middle zoom-in).

Post-Process Depth of Field. Earlier, we discussed our approach’s integration with FXAA, a commonly used post-process in modern game engines. Another commonly used post-process effect is depth of field (DoF); however, the combination of DoF and motion blur post-processes is a subject of little investigation. We implemented the post-process DoF approach of Gilham in ShaderX5 [Eng06] and briefly discuss its interaction with our motion blur filter. Specifically, the correct order in which to apply the two filters is not

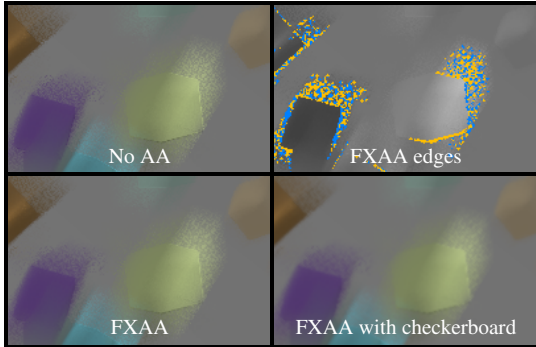


Figure 13: Our noise is well-suited for standard post-process FXAA edge-detection, and we can further “hint” FXAA using a pixel-frequency luminance checkerboard.

immediately apparent. We experimented with both options and illustrate our results in an especially difficult scene, as far as motion and DoF complexity are concerned: three distinctly colored wheels, each undergoing different rotational motion, at three different depths, and with the focus on the green middle wheel (see Figure 14).

The differences are subtle and our experiments far from comprehensive, however we note (somewhat counter-intuitively) that applying DoF *after* motion blur yields fewer visible edges in blurred regions and sharper features on in-focus regions. Applying DoF after motion blur has the added benefit of further blurring our noise artifacts.

6. Conclusions and Future Work

We presented a high-performance post-process motion blur filter that is robust to scenes with complex inter-object motions and fine-scale details. We demonstrated our approach on several such scenes with clear quality benefits, both in images and in animation (see the supplemental video), and at a negligible cost compared to the state-of-the-art. Our approach is temporally coherent, easy to integrate, and readily compatible with other commonly used post-process effects. Some interesting avenues of future work include a more in-depth analysis of the interaction and combination of DoF and motion blur post-processes, as well as extending our ideas to more flexible rendering architectures, such as stochastic rasterization or micropolygon renderers.

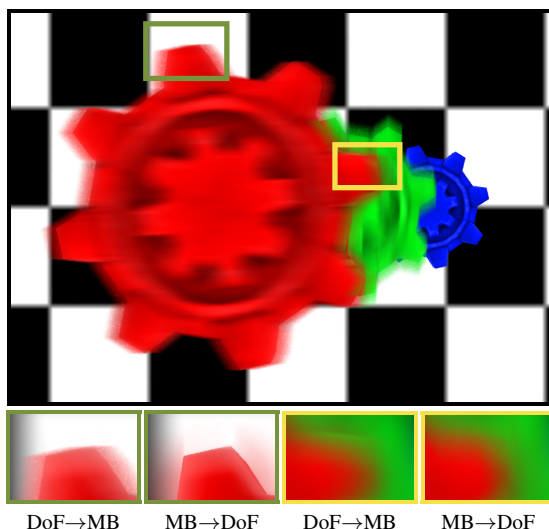


Figure 14: DoF and motion blur stress test. Top: Motion blur alone. Bottom: Comparison of motion blur and depth of field ordering. We note slightly better results when DoF is applied after motion blur.

References

- [AMMH07] AKENINE-MÖLLER T., MUNKBERG J., HASSELGREN J.: Stochastic rasterization using time-continuous triangles. In *Graphics Hardware* (2007), Eurographics, pp. 7–16. 2
- [Coo86] COOK R. L.: Stochastic sampling in computer graphics. *ACM Trans. Graph.* 5, 1 (1986), 51–72. 1, 2
- [Eng06] ENGEL W.: *Shader X5: Advanced Rendering Techniques*. Charles River Media, MA, USA, 2006. 1, 7
- [ETH*09] EGAN K., TSENG Y.-T., HOLZSCHUCH N., DURAND F., RAMAMOORTHY R.: Frequency analysis and sheared reconstruction for rendering motion blur. *ACM Trans. Graph.* 28, 3 (2009). 1, 2
- [FLB*09] FATAHALIAN K., LUONG E., BOULOS S., AKELEY K., MARK W. R., HANRAHAN P.: Data-parallel rasterization of micropolygons with defocus and motion blur. In *High Performance Graphics* (2009), ACM, pp. 59–68. 2
- [HJW*08] HACHISUKA T., JAROSZ W., WEISTROFFER R. P., DALE K., HUMPHREYS G., ZWICKER M., JENSEN H. W.: Multidimensional adaptive sampling and reconstruction for ray tracing. *ACM Trans. Graph.* 27, 3 (2008). 2
- [KS11] KASYAN N., SCHULZ N.: Secrets of cryengine 3 graphics technology. In *SIGGRAPH Talks*. ACM, 2011. 2
- [LAC*11] LEHTINEN J., AILA T., CHEN J., LAINE S., DURAND F.: Temporal light field reconstruction for rendering distribution effects. *ACM Trans. Graph.* 30, 4 (2011), 55. 1, 2
- [Len10] LENGYEL E.: Motion blur and the velocity-depth-gradient buffer. In *Game Engine Gems*, Lengyel E., (Ed.). Jones & Bartlett Publishers, March 2010. 2, 3, 4
- [Lot09] LOTTES T.: Fast approximate anti-aliasing (fxaa). 2009. URL: http://developer.download.nvidia.com/assets/gamedev/files/sdk/11/FXAA_WhitePaper.pdf. 1
- [Lov05] LOVISCACH J.: Motion blur for textures by means of anisotropic filtering. *EGSR*, pp. 105–110. 2
- [MESL10] MCGUIRE M., ENDERTON E., SHIRLEY P., LUEBKE D. P.: Real-time stochastic rasterization on conventional GPU architectures. In *High Performance Graphics* (2010). 2
- [MHBO12] MCGUIRE M., HENNESSY P., BUKOWSKI M., OSMAN B.: A reconstruction filter for plausible motion blur. In *13D* (2012), pp. 135–142. 1, 2, 3, 4, 6, 7, 10
- [ML85] MAX N. L., LERNER D. M.: A two-and-a-half-d motion-blur algorithm. In *Proceedings of the 12th annual conference on Computer graphics and interactive techniques* (New York, USA, 1985), SIGGRAPH '85, ACM, pp. 85–93. 2
- [NSG11] NAVARRO F., SERÓN F. J., GUTIERREZ D.: Motion blur rendering: State of the art. *Computer Graphics Forum* 30, 1 (2011), 3–26. 2
- [ODR09] OVERBECK R. S., DONNER C., RAMAMOORTHY R.: Adaptive wavelet rendering. *ACM Trans. Graph.* 28, 5 (2009). 2
- [Pep03] PEPPER D.: Per-pixel motion blur for wheels. In *ShaderX6*, Engel W., (Ed.). Charles River Media, 2003. 2
- [RAMN12] RAMAMOORTHY R., ANDERSON J., MEYER M., NOWROUZEZAHRAI D.: A theory of monte carlo visibility sampling. *ACM Transactions on Graphics* (2012). 6
- [RMM10] RITCHIE M., MODERN G., MITCHELL K.: Split second motion blur. In *SIGGRAPH 2010 Talks* (NY, USA, 2010), ACM. 2
- [Ros08] ROSADO G.: Motion blur as a post-processing effect. In *GPU Gems 3*. Addison-Wesley, 2008, pp. 575–581. 2

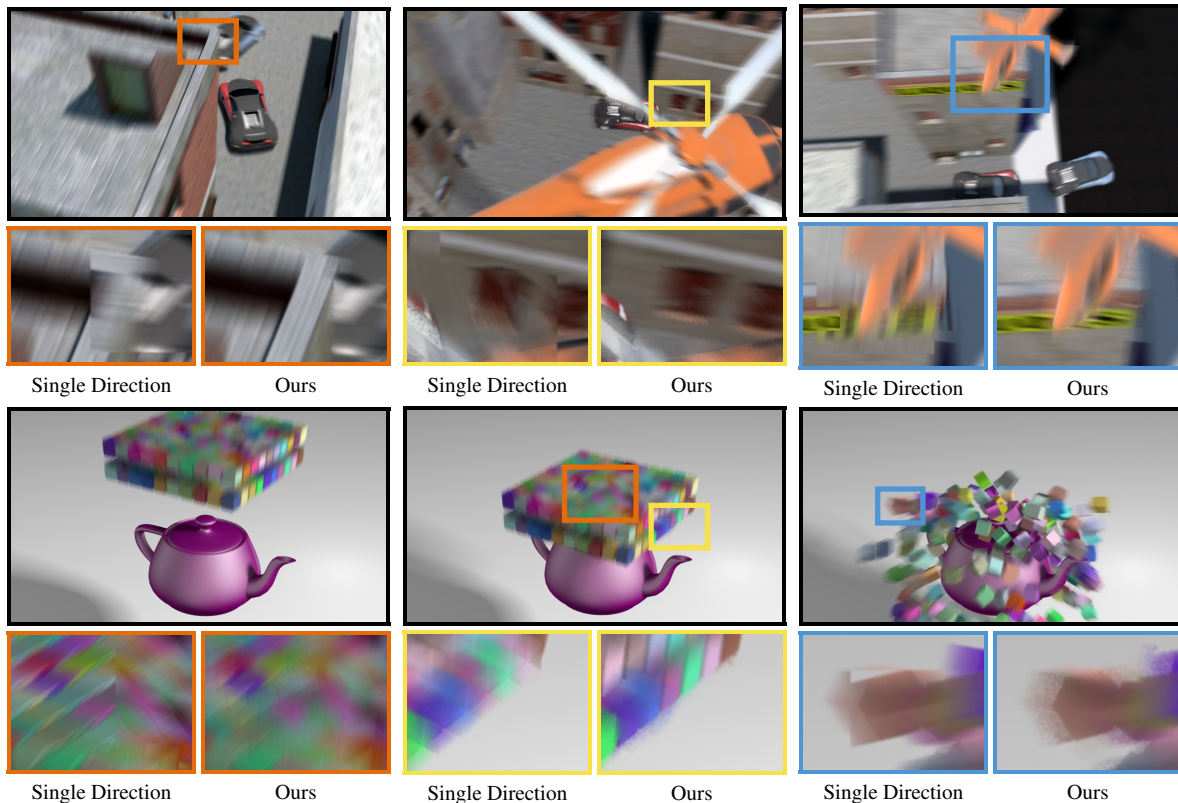


Figure 15: Our results are temporally stable on complex scenes where previous approaches suffer from distracting artifacts.

- [SAC*11] SHIRLEY P., AILA T., COHEN J. D., ENDERTON E., LAINE S., LUEBKE D. P., MCGUIRE M.: A local image reconstruction algorithm for stochastic rendering. In *ISD* (2011), pp. 9–14. 2, 3
- [SD12] SEN P., DARABI S.: On filtering the noise from the random parameters in monte carlo rendering. *ACM Trans. Graph.* 31, 3 (2012), 18. 2
- [Sou11] SOUSA T.: Cryengine 3 rendering techniques. In *Microsoft Game Technology Conference*. August 2011. 2
- [Sou13] SOUSA T.: Graphics gems from cryengine 3. In *ACM SIGGRAPH Course Notes* (2013). 1, 2, 3, 4, 7
- [TBI03] TATARCHUK N., BRENNAN C., ISIDORO J. R.: Motion blur using geometry and shading distortion. In *ShaderX2: Shader Programming Tips and Tricks with DirectX 9.0*, Engel W., (Ed.). 2003. 2
- [WLH97] WONG T.-T., LUK W.-S., HENG P.-A.: Sampling with hammersley and halton points. *J. Graph. Tools* 2, 2 (1997), 9–24. 6
- [ZG12] ZIOMA R., GREEN S.: Mastering DirectX 11 with Unity, March 2012. Presentation at GDC 2012 https://developer.nvidia.com/sites/default/files/akamai/gamedev/files/gdc12/GDC2012_Mastering_DirectX11_with_Unity.pdf. 2, 3, 4

Acknowledgements

The NeighborMax tile culling algorithm was contributed by Dan Evangelakos at Williams College. Observations about FXAA, the use of the luminance checkerboard, and considering the central velocity in the gather kernel are from our colleagues at Vicarious Visions: Padraic Hennessy, Brian Osman, Michael Bukowski.

Appendix A: Pseudocode

We include pseudocode that depends on the following helper functions and shorthand operators: `sOffset` jitters a tile lookup (but never into a diagonal tile), `rnmix` is a vector linear interpolation followed by normalization, `norm` returns a normalized vector, `⌊·⌋` returns the whole component, and `&` denotes bitwise **and**. Unless otherwise specified, we use the notation/functions of McGuire et al. [MHBO12]. Our function returns **four** values: the filtered color and luminance value to pass to an optional FXAA post-process.

```

function filter(p):
  let  $j = \text{halton}(-1, 1)$ 
  let  $\mathbf{v}_{\max} = \text{NeighborMax}[\mathbf{p}/r + \text{sOffset}(\mathbf{p}, j)]$ 
  if ( $\|\mathbf{v}_{\max}\| \leq 0.5$ )
    return ( $\text{color}[\mathbf{X}], \text{luma}(\text{color}[\mathbf{X}])$ )

  let  $\mathbf{w}_n = \text{norm}(\mathbf{v}_{\max}), \mathbf{v}_c = \mathbf{V}[\mathbf{p}]$ ,
     $\hookrightarrow \mathbf{w}_p = (-w_{ny}, w_{nx})$ 
  if ( $\mathbf{w}_p \cdot \mathbf{v}_c < 0$ )  $\mathbf{w}_p = -\mathbf{w}_p$ 
  let  $\mathbf{w}_c = \text{rnmix}(\mathbf{w}_p, \text{norm}(\mathbf{v}_c), (\|\mathbf{v}_c\| - 0.5)/\gamma)$ 

  // Begin integration with the current point
  // (center weight) p
  let  $\text{totalWeight} = N/(\kappa \times \|\mathbf{v}_c\|)$ 
  let  $\text{result} = \text{color}[\mathbf{p}] \times \text{totalWeight}$ 

```

```

for  $i \in [0, N)$ 
  let  $t = \text{mix}(-1, 1, (i + j \times \eta + 1)/(N + 1))$  // jitter
    our sample

  // Compute the sample point S; split samples
  // between  $\{\mathbf{v}_{\max}, \mathbf{v}_c\}$ 
  let  $\mathbf{d} = \mathbf{v}_c$  if  $i$  odd or  $\mathbf{v}_{\max}$  if  $i$  even
  let  $\mathbf{T} = t \times \|\mathbf{v}_{\max}\|$ 
  let  $\mathbf{S} = \lfloor t \times \mathbf{d} \rfloor + \mathbf{p}$ 

  // Compute S's velocity and color
  let  $\mathbf{v}_s = \mathbf{V}[\mathbf{S}], \text{colorSample} = \text{color}[\mathbf{S}]$ 

  // Fore- vs. background classification of Y
  // relative to p
  let  $f = \text{zCompare}(\mathbf{Z}[\mathbf{p}], \mathbf{Z}[\mathbf{S}])$ 
  let  $b = \text{zCompare}(\mathbf{Z}[\mathbf{S}], \mathbf{Z}[\mathbf{p}])$ 

  // This sample's weight and velocity-aware factors
  // (Section 4.1)
  let  $\text{weight} = 0, w_A = \mathbf{w}_c \cdot \mathbf{d}, w_B = \text{norm}(\mathbf{v}_s) \cdot \mathbf{d}$ 

  // The three phenomenological cases
  // (Sections 3 and 4.1):
  // Objects moving over p, blur from p's motion,
  // and their blending
   $\text{weight} += f \cdot \text{cone}(\mathbf{T}, 1/\|\mathbf{v}_s\|) \times w_B$ 
   $\text{weight} += b \cdot \text{cone}(\mathbf{T}, 1/\|\mathbf{v}_c\|) \times w_A$ 
   $\text{weight} += \text{cylinder}(\mathbf{T}, \min(\|\mathbf{v}_s\|, \|\mathbf{v}_c\|))$ 
     $\hookrightarrow \times \max(w_A, w_B) \times 2$ 

   $\text{totalWeight} += \text{weight}$  // For normalization
   $\text{result} += \text{colorSample} \times \text{weight}$ 

return ( $\text{result}/\text{totalWeight}, (\mathbf{p}_x + \mathbf{p}_y) \& 1$ )

```